ARTICLE

Second Nearest-Neighbor Modified Embedded Atom Method Interatomic Potential for Cu-Ni-Sn Ternary System

Jialiang Dong[1,2], Xuemao Dong[3,4], Zhongxue Feng[3,4,*], Caiju Li[3,4], Jianhong Yi[3,4] and Jun Tan[5,*]

[1]School of Materials Science and Engineering, Guizhou Minzu University, Guiyang, 550025, China
[2]Guangdong Key Laboratory for Advanced Metallic Materials Processing and Forming, National Engineering Research Center of Near-Net-Shape Forming for Metallic Materials, South China University of Technology, Guangzhou, 510640, China
[3]Faculty of Electronic and Information Engineering, Anshun University, Anshun, 561000, China
[4]Faculty of Materials Science and Engineering, Kunming University of Science and Technology, Kunming, 650093, China
[5]College of Materials Science and Engineering, Chongqing University, Chongqing, 400044, China
*Corresponding Authors: Zhongxue Feng. Email: fzxue2003@163.com; Jun Tan. Email: j.tan@cqu.edu.cn

ABSTRACT: To explore atomic-level phenomena in the Cu-Ni-Sn alloy, a second nearest-neighbor modified embedded-atom method (2NN MEAM) potential has been developed for the Cu-Ni-Sn system, building upon the work of other researchers. This potential demonstrates remarkable accuracy in predicting the lattice constant, with a relative error of less than 0.5% when compared to density functional theory (DFT) results, and it achieves a 10% relative error in the enthalpy of formation compared to experimental data, marking substantial advancements over prior models. The bulk modulus is predicted with a relative error of 8% compared to DFT. Notably, the potential effectively simulates the processes of melting and solidification of Cu-15Ni-8Sn, with a simulated melting point that closely aligns with the experimental value, within a 7.5% margin. This serves as a foundation for establishing a 2NN MEAM potential for a flawless Cu-Ni-Sn system and its microalloying systems.

KEYWORDS: 2NN MEAM; Cu-Ni-Sn; interatomic potential; atomistic simulation

1 Introduction

Cu-Ni-Sn alloys have garnered significant attention due to their non-toxicity, low cost, and superior mechanical properties [1–5], among these, Cu-15Ni-8Sn alloys are particularly notable for their exceptional high strength and elastic modulus, with applications in electronic parts, maritime engineering, and aerospace [6,7]. However, the low melting point of Sn (504.89 K) compared to Ni (1726 K) and Cu (1356.4 K) leads to severe macroscopic segregation during solidification, which can weaken the alloy's properties and limit its applications [8]. To mitigate segregation, it is essential to study the macro-segregation behaviors and mechanisms in detail, which requires the study of the atomic behaviors between different elements during the crystallization process, both through experiments and atomistic simulations. But conducting accurate and specific experiments is difficult due to the need for real-time, high-resolution, and high-temperature atomic measurements. Regarding this situation, the atomistic simulation study can provide an efficient and powerful method to study atomic behaviors.

Among the various atomic simulation methods, density functional theory (DFT) based on first-principle calculations can accurately predict atomic behaviors and material properties [9]. However, DFT is

computationally intensive and only suitable for small-scale atomic simulations (hundreds of atoms), making it impractical for large-scale simulations such as those involving solidification processes. In contrast, the Molecular Dynamics (MD) method is effective for simulating large-scale atomic systems and predicting their properties [10,11]. MD simulations based on the second nearest-neighbor modified embedded-atom method (2NN MEAM) potentials [12–15] have been successfully applied to various systems, including Mg-Zn-Ca [16], FeCo [17], NiTi [18], Cu-Ni [19], Cu-Sn [20–22], Ni-Sn [20], Cu [21], Ni [23], and Sn [24], among others. These simulations have reasonably predicted the fundamental behaviors of materials. However, no reports exist on the development of a 2NN MEAM potential for the Cu-Ni-Sn system.

In this work, we developed a 2NN MEAM interatomic potential for the Cu-Ni-Sn ternary system based on existing unary and binary interatomic parameters. First, the accuracy of this potential was verified by DFT. Subsequently, the potential was used to simulate the melting process and XRD patterns of Cu-15Ni-8Sn, and the results were compared with experimental data to evaluate the rationality of the potential parameters.

2 Methods

2.1 Potential Formalism

The MEAM formalism has been comprehensively and formally explained in previous articles [25–30]. In the modified 2NN MEAM [31,32] formula, the second nearest-neighbor interaction is considered, which is affected by the adjustment of the screening parameter, making the many-body screening (S_{ij}) less serious. The total energy of each atom is computed using Eq. (1) [33].

$$E^u(R) = F\left(\overline{\rho^0}(R)\right) + \frac{Z_1}{2}\varnothing(R) + \frac{Z_2 S_{ij}}{2}\varnothing(aR), \tag{1}$$

where Z_1 and Z_2 are the atom numbers of the first and second nearest-neighbors, respectively. a denotes the ratio of the distance between the second and first nearest-neighbor atoms.

The basic idea for the screening is that if atom k exceeds the C_{max} defined ellipse, it is considered to have no influence on the interaction between atoms i and j. If atom k is within a C_{min} defined ellipse, it is considered to completely shield the interaction between atoms i and j. If atom k is within C_{max} and C_{min}, then the screening effect varies gradually, as shown in Fig. 1. According to the relative distances among the three atoms (i, j, and k), the values of the parameters C, C_{min}, and C_{max} are calculated.
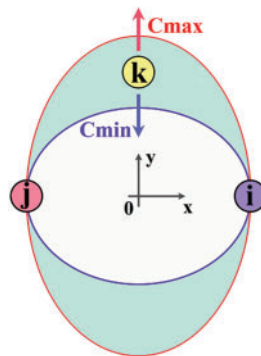
Figure 1: The screening schematic diagram of the three cases for the ternary system. In this diagram, the symbols i, j, and k correspond to Cu, Ni, and Sn, respectively

For each atom, the total energy value $E^u(R)$ can be calculated via the zero-temperature universal equation of state developed by Rose et al. [27]. The equation is written as below:

$$E^u(R) = -E_c(1 + a^* + da^{*3})e^{-a^*},\qquad(2)$$

where d represents an adjustable parameter,

$$a^* = \alpha\left(\frac{R}{r_e} - 1\right),\qquad(3)$$

$$\alpha = \left(\frac{9B\Omega}{r_e}\right)^{\frac{1}{2}}.\qquad(4)$$

In Eqs. (2)–(4), the cohesive energy E_c is measured and expressed in the unit of eV/atom; the r_e, denoting equilibrium nearest-neighbor distance, is expressed in å; the bulk modulus B is measured in 10^{12} dyne/cm^2, and Ω represent the atomic volume.

2.2 Development of the Cu-Ni-Sn Ternary 2NN MEAM Potentials

The 2NN MEAM potential for ternary system is derived from the unary and binary potentials, incorporating three $C_{min}^{(i-k-j)}$ and three $C_{max}^{(i-k-j)}$ ternary parameters. In this paper, the 2NN MEAM potential for Cu-Ni-Sn is established by using the existing parameters of the unary and binary potentials, as shown in Tables 1 and 2, respectively.

Table 1: 2NN MEAM potential parameter sets for the Cu, Ni, and Sn unary systems [20]

Element	E_c	r_e	B	$\AA$	$\beta^{(0)}$	$\beta^{(1)}$	$\beta^{(2)}$	$\beta^{(3)}$	$t^{(1)}$	$t^{(2)}$	$t^{(3)}$	C_{min}	C_{max}	d
Cu	3.54	2.555	1.2818	0.73	2.54	2.24	1.48	0.14	1.46	1.88	1.20	0.21	1.29	0.10
Ni	4.45	2.490	1.8759	0.94	2.56	1.50	6.00	1.50	3.10	1.80	4.36	0.81	2.80	0.05
Sn	3.05	3.480	0.6088	1.05	5.50	5.10	4.50	4.30	1.30	3.60	−0.90	1.29	4.43	0.02

Table 2: 2NN MEAM potential parameter sets for the Cu-Ni [19], Cu-Sn and Ni-Sn [20] binary systems

	Cu-Ni	Cu-Sn	Ni-Sn
Reference	Ll$_2$ CuNi$_3$	CsCl type CuSn	Ll$_2$ Ni$_3$Sn
E_c	4.2225	3.2450	4.2920
r_e	2.507	2.920	2.7764
B	1.727	0.8011	1.7271
$C_{min}^{(X-Y-X)}$	1.00	0.27	0.30
$C_{min}^{(Y-X-Y)}$	1.00	0.17	2.27
$C_{min}^{(X-X-Y)}$	1.21	0.07	0.51
$C_{min}^{(X-Y-Y)}$	1.00	0.14	0.66
$C_{max}^{(X-Y-X)}$	2.80	1.93	1.68
$C_{max}^{(Y-X-Y)}$	2.80	1.15	2.61
$C_{max}^{(X-X-Y)}$	2.80	2.36	1.56

(Continued)

Table 2 (continued)

	Cu-Ni	Cu-Sn	Ni-Sn
$C_{max}^{(X-Y-Y)}$	2.80	3.41	1.78
d	0.06	0.06	0.03
$\rho_0^X:\rho_0^Y$	1:1	1:1	1.17:0.7

For the parameters $C_{min/max}^{(i-k-j)}$, if two elements (i and j) exhibit a degree of similarity to a third element (k), it is assumed that the screening degree of screening by k (or j) atom to the interaction between i and j (or k) atoms [$C_{min/max}^{(i-k-j)}$ or $C_{min/max}^{(i-j-k)}$] is the average between those to the i-k [$C_{min/max}^{(i-k-k)}$] and $i-j$ [$C_{min/max}^{(i-j-j)}$] interactions. This assumption has been used in the establishment of 2NN MEAM potentials for ternary systems and can accurately predict the basic material properties of alloys such as Mg-Al/Zn-Ga [12], Fe-Ti/Nb-C/N [34,35], V-Pd-Y [36], Fe-Cr-Ni [37] and Na-M-Sn (M=Cu, Mn, Ni) [20] systems. Therefore, to develop the Cu-Ni-Sn system, it is assumed that Cu, Ni, and Sn with FCC structure are relatively similar, and then ternary parameters $C_{min/max}^{(i-k-j)}$ can be determined automatically based on the potential parameters of the binary system, as shown in Table 3.

Table 3: 2NN MEAM potential parameter sets for the three $C_{min}^{(i-k-j)}$ and three $C_{max}^{(i-k-j)}$ ternary parameters

Parameter	Selected value	Procedure for determination
$C_{min}^{(Cu-Sn-Ni)}$	0.47	$\left[0.5\left(C_{min}^{Cu-Sn-Sn}\right)^{\frac{1}{2}} + 0.5\left(C_{min}^{Cu-Ni-Ni}\right)^{\frac{1}{2}}\right]^2$
$C_{min}^{(Sn-Cu-Ni)}$	0.47	$\left[0.5\left(C_{min}^{Sn-Cu-Cu}\right)^{\frac{1}{2}} + 0.5\left(C_{min}^{Sn-Ni-Ni}\right)^{\frac{1}{2}}\right]^2$
$C_{min}^{(Ni-Sn-Cu)}$	0.82	$\left[0.5\left(C_{min}^{Ni-Sn-Sn}\right)^{\frac{1}{2}} + 0.5\left(C_{min}^{Ni-Cu-Cu}\right)^{\frac{1}{2}}\right]^2$
$C_{max}^{(Cu-Sn-Ni)}$	3.10	$\left[0.5\left(C_{max}^{Cu-Sn-Sn}\right)^{\frac{1}{2}} + 0.5\left(C_{max}^{Cu-Ni-Ni}\right)^{\frac{1}{2}}\right]^2$
$C_{max}^{(Cu-Ni-Sn)}$	3.10	$\left[0.5\left(C_{max}^{Cu-Ni-Ni}\right)^{\frac{1}{2}} + 0.5\left(C_{max}^{Cu-Sn-Sn}\right)^{\frac{1}{2}}\right]^2$
$C_{max}^{(Ni-Sn-Cu)}$	3.10	$\left[0.5\left(C_{max}^{Ni-Sn-Sn}\right)^{\frac{1}{2}} + 0.5\left(C_{max}^{Ni-Cu-Cu}\right)^{\frac{1}{2}}\right]^2$

2.3 Calculation Procedures

To validate the potential, the fundamental material properties of different Cu-Ni-Sn compounds computed by MD and DFT were compared. Furthermore, the MD simulation of melting and solidification process of the Cu-15Ni-8Sn alloy was compared with the experimental data to confirm the potential's applicability. The simulations included energy minimization, equilibration steps (10 ps at 300 K), and heating/cooling steps (heating rate of 1 K/ps from 300 K to 2500 K and cooling rates of 1 K/ps back to 300 K, respectively). Large-scale atomic/molecular massively parallel simulator (LAMMPS) [38] is used for MD simulations, and the potentials used in the calculations are the ones established in this paper. The velocity Verlet algorithm was employed to unify Newton's equations of motion. The timestep used was 1 fs. The simulations were performed in the NVT ensemble (constant number of particles, constant volume, constant temperature). The atom types and phase structures were identified using the OVITO software [39]. The Vienna *Ab initio* Simulation Package (VASP) [40−42] was used to the calculate DFT, which were based on

the Projector Augmented-Wave (PAW) method [43], and the improved Perdew-Burke-Ernzerhof (PBE) [44] gradient was used to estimate the exchange-correlation function. The energy cutoff (E_{cut}) for plane-wave basis set was at 400 eV. Dense k-point meshes in the first Brillouin zone with a Monkhorst-Pack scheme were employed, with a sample of 8*8*8 for each structure mentioned above.

2.4 Experimental Procedures

Cu-15Ni-8Sn alloy was obtained using vacuum induction melting using high-purity electrolytic copper (99.99 wt.%), electrolytic Ni (99.99 wt.%), and industrial pure Sn (99.99 wt.%). As indicated by the pseudo-binary phase diagram (Fig. 2) of the Cu-15Ni-8Sn alloy [45], the alloy exhibits a melting point of approximately 1400 K. The precise chemical composition is detailed in Table 4.
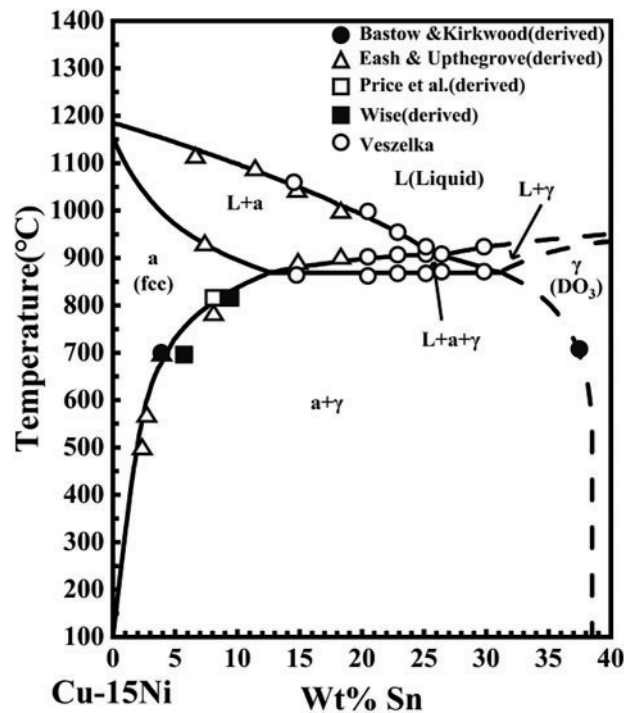
Figure 2: Pseudo-binary phase diagram of Cu-Ni-Sn (at the isopleth of 15 wt.% Ni) alloy

Table 4: Chemical compositions of the Cu-15Ni-8Sn alloy (wt.%)

Measured composition	Ni	Sn	Cu
Cu-15Ni-8Sn	15.49	8.52	Balance

Test samples were extracted from the ingot center. The metallographic sample surfaces were polished suing abrasive SiC papers and subsequently etched with a solution composed of 95 mL C_2H_5OH, 5 mL HCl, 5 g $FeCl_3$ to reveal the microstructure under scanning electron microscopy (SEM). The materials' phase structure was characterized using XRD analytical, utilizing Cu-Ka radiation within the 20° to 100° (2θ) range at a scan rate of 10°/min. The resultant data were processed utilizing JADE software.

3 Results and Discussion

3.1 Cu-Ni-Sn Ternary System Property Parameters and Contrast with DFT

To verify e the reliability of the established ternary potential parameters, the property parameters (lattice constant, bulk modulus, and enthalpy of formation) for the compounds Cu_2NiSn and $CuNi_2Sn$ in Cu-Ni-Sn alloys were calculated by MD and compared to the DFT calculation results. Fig. 3 displays all the computed fitted E-V curves, where all data points are compatible with the third-order Birch-Murnaghan equation of state (EOS, as shown in Eq. (5)) [46,47].

$$E(V) = E_0 + \frac{9V_0B_0}{16}\left\{\left[\left(\frac{V_0}{V}\right)^{\frac{2}{3}} - 1\right]^3 B_0' + \left[\left(\frac{V_0}{V}\right)^{\frac{2}{3}} - 1\right]^2 \left[6 - 4\left(\frac{V_0}{V}\right)^{\frac{2}{3}}\right]\right\}, \tag{5}$$

where E_0 is the total energy per unit cell at zero pressure, B_0 and B_0' represent bulk modulus and the first-order pressure derivatives of bulk modulus, respectively. V_0 and V represent the reference volume and deformation volume, respectively.
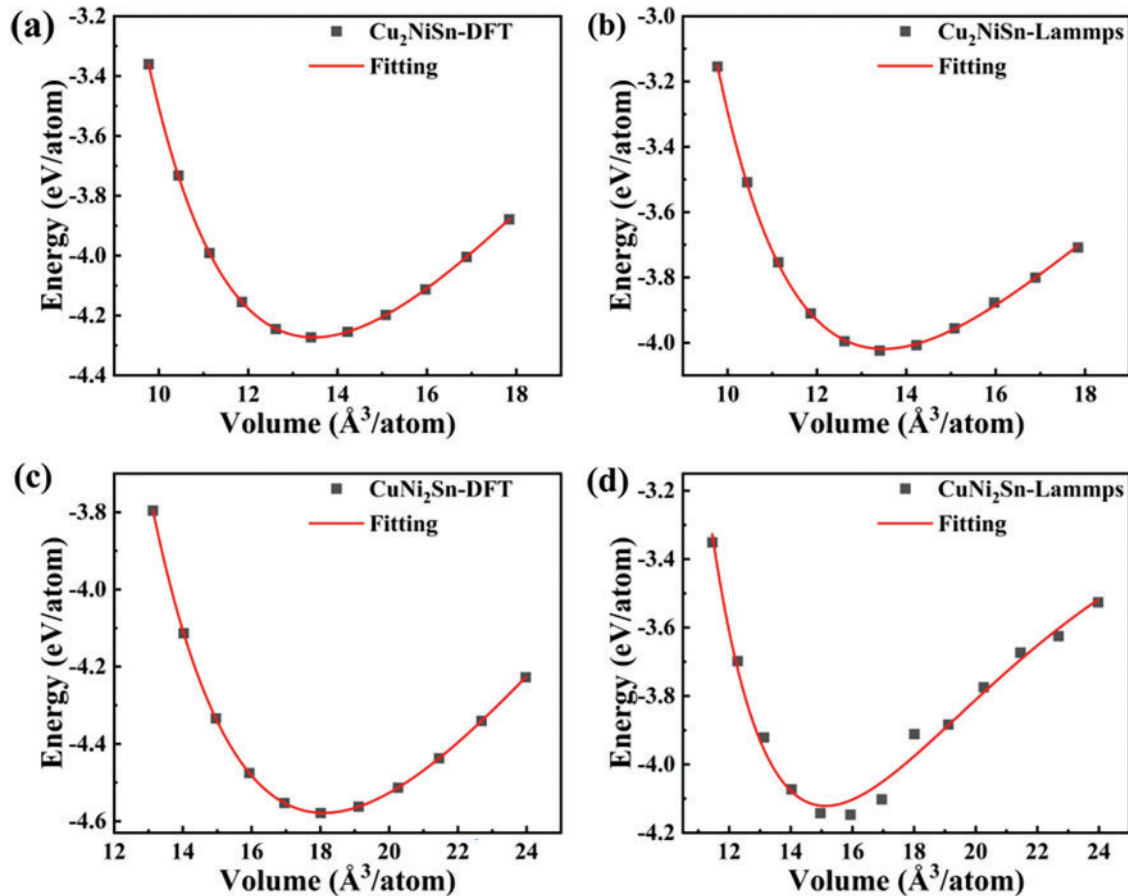
Figure 3: The E-V curves of different Cu-Ni-Sn intermetallic compounds were calculated by DFT and MD. (a) The Cu_2NiSn by DFT calculation, (b) The Cu_2NiSn by MD calculation, (c) The $CuNi_2Sn$ by DFT calculation, and (d) The $CuNi_2Sn$ by MD calculation

The results of the property parameters of Cu-Ni-Sn ternary compounds calculated by DFT and MD are shown in Table 5. The lattice constants and bulk modulus calculated by MD are consistent with those calculated by DFT. This indicates that the potential parameter can effectively reproduce the atomic simulation of the ternary system, thereby confirming the feasibility of this parameter.

Table 5: The property parameters (the lattice constant a (Å), the enthalpy of formation $\triangle E_f$ (eV/atom), the bulk V (Å^3/atom), and the bulk modulus B (10^{12} dyne/cm^2)) of Cu-Ni-Sn intermetallic compounds were calculated by using 2NN MEAM potential, and the comparison with those calculated by DFT

Compound	Structure	Property	DFT	2NN MEAM	Relative error
Cu_2NiSn	$Fm\overline{3}m$	a	5.994902	5.997783	0.048%
		$\triangle E_f$	−0.03025	−0.03799	25.59%
		V	13.46562	13.48504	0.14%
		B	0.96203	0.83486	13.22%
$CuNi_2Sn$	$Fm\overline{3}m$	a	6.615983	6.232149	5.80%
		$\triangle E_f$	−0.089395	−0.183445	105.15%
		V	18.09936	15.12842	16.41%
		B	0.62639	0.85578	36.59%

3.2 Comparison of Simulation and Experimental Results of the Melting and Solidification Processes of Cu-15Ni-8Sn Alloy

The melting and solidification behaviors of the Cu-15Ni-8Sn alloy were investigated via molecular dynamics (MD) simulations, utilizing the established potential to determine the simulated melting point, XRD patterns, and Sn segregation during solidification. To facilitate the statistical analysis of Sn fractions at grain boundaries, a random substitution atom model based on a symmetric grain boundary structure was constructed. The atomic model, depicted in Fig. 4a, comprises 5760 atoms, of which 273 are Sn atoms. The structural model is illustrated in Fig. 4b, where the white regions represent the grain boundaries. The system was initially equilibrated at a temperature of 300 K and a pressure of 0 bar, subsequently heated to 2500 K, and then cooled back to 300 K. The grain boundary region is defined based on the atomic coordinates and the Voronoi tessellation method. Atoms with a high number of Voronoi faces (typically more than 7) were identified as grain boundary atoms. Simulated snapshots capturing the structural evolution during the solidification process are presented in Fig. 4c and d.

The average potential energy—temperature curve (as shown in Fig. 5a) indicates that the potential energy of the Cu-15Ni-8Sn alloy undergoes significant changes at ~1140 K during the heating stage and at ~1850 K during the cooling stage The molecular dynamics simulations were conducted with a heating rate of 1 K/ps and a cooling rate of 0.5 K/ps. Furthermore, it suggests that at low temperatures, the configuration during heating stage has a higher energy than that during cooling stage. This finding highlights that the initial configuration during heating possess higher energy, whereas the configuration during cooling process is characterized by lower energy. These observations provide crucial insights into the phase transition and structural evolution of the Cu-15Ni-8Sn alloy, aligning well with the fundamental physical processes of thermal activation, structural rearrangement, and solidification.
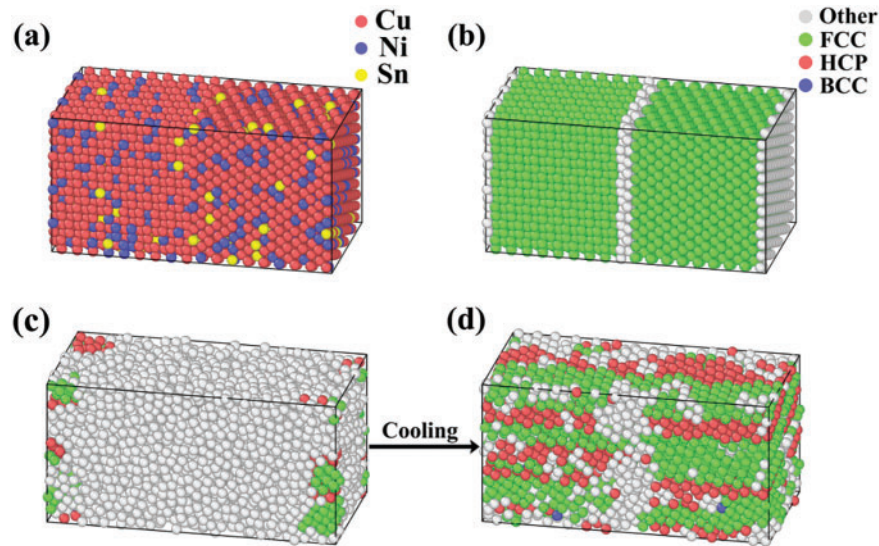
Figure 4: (a) atomic model of the Cu-15Ni-8Sn alloys at initial; (b) structural model of the Cu-15Ni-8Sn alloys at initial; (c) simulation snapshot at 1140 K during solidification; (d) simulation snapshot at 1092 K during solidification
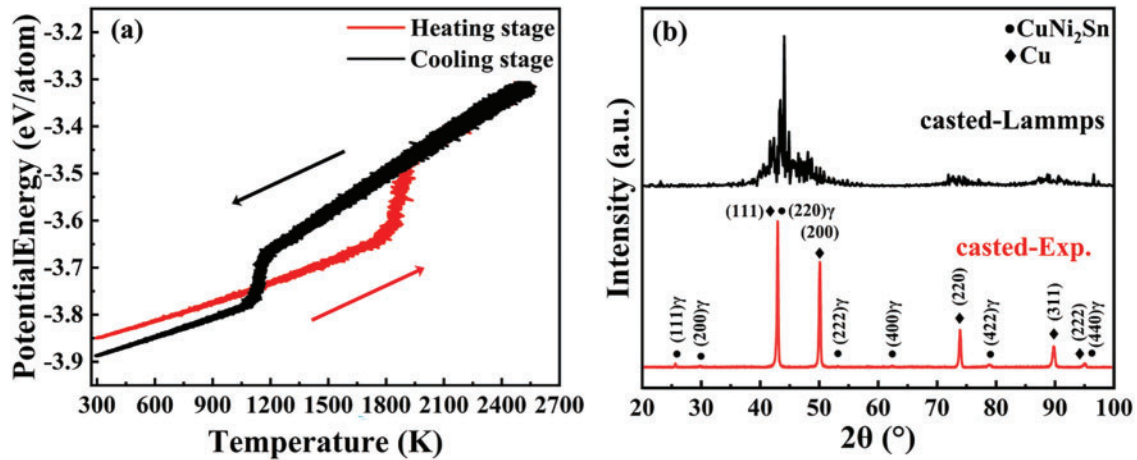
Figure 5: (a) The 2NN MEAM potential was employed to simulate the temperature-dependent variation of potential energy for the Cu-15Ni-8Sn alloy. (b) XRD of Cu-15Ni-8Sn alloy samples cast Experiment and MD simulation

Based on Eq. (6) [48–51], the simulated melting point of the Cu-15Ni-8Sn alloy is approximately 1538 K, which corresponds to a maximum deviation of about 9.8% from the melting point reported in Fig. 2 (approximately 1400 K). Fig. 5b presents the XRD results, which demonstrate a strong correlation between the simulated and experimental data, thereby validating the accuracy and reliability of the simulation approach.

$$T_m = T_H + T_C - \sqrt[2]{T_H * T_C}, \tag{6}$$

where T_m represents the simulated melting point, whereas T_H and T_C refer to the temperature at which there is a sudden change in potential energy during superheating and supercooling, respectively.

An investigation was conducted on the relationship between temperature and the Sn proportions at grain boundary during the solidification, and the proportion of Sn at the grain boundaries was recorded every 1000 steps, as shown in Fig. 6. Among them, the proportion of Sn atoms in the grain boundary tends to increase with temperature decreasing and increases sharply at 1140 K. It is evident that Sn enrichment occurs at grain boundaries during the solidification.
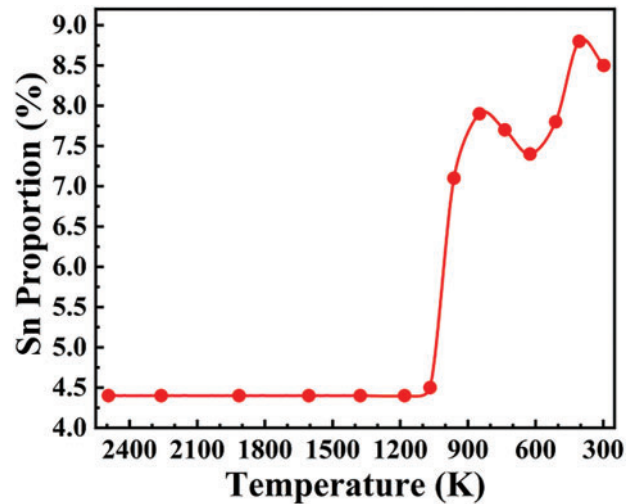
Figure 6: The proportion of Sn at grain boundaries during solidification for the Cu-15Ni-8Sn alloy

The microstructure of the as-cast Cu-15Ni-8Sn alloy is illustrated in Fig. 7a. The alloy displays a typical dendritic structure, which is composed of three main components: a dark dendritic matrix (α-Cu), a white irregular structure (γ-DO$_3$), and a grey interdendritic region (coexistence of α and γ phases). The corresponding EDS results are summarized in Table 6. The Sn content in the α-matrix is 6.41 wt.%, which is 2.1 wt.% lower than the average value of the alloy (8.52 wt.%). In contrast, the Sn content in both the white irregular γ phase and the lamellar γ phase is higher than the average value of the alloy. Notably, the γ phase adopts a white irregular morphology when the Sn content exceeds a critical value of approximately 39.44 wt.%.

In summary, the established potential has good applicability for simulating the melting and solidification processes of the Cu-15Ni-8Sn alloy. However, the differences may exist when applying other simulations, and further optimization is still needed.
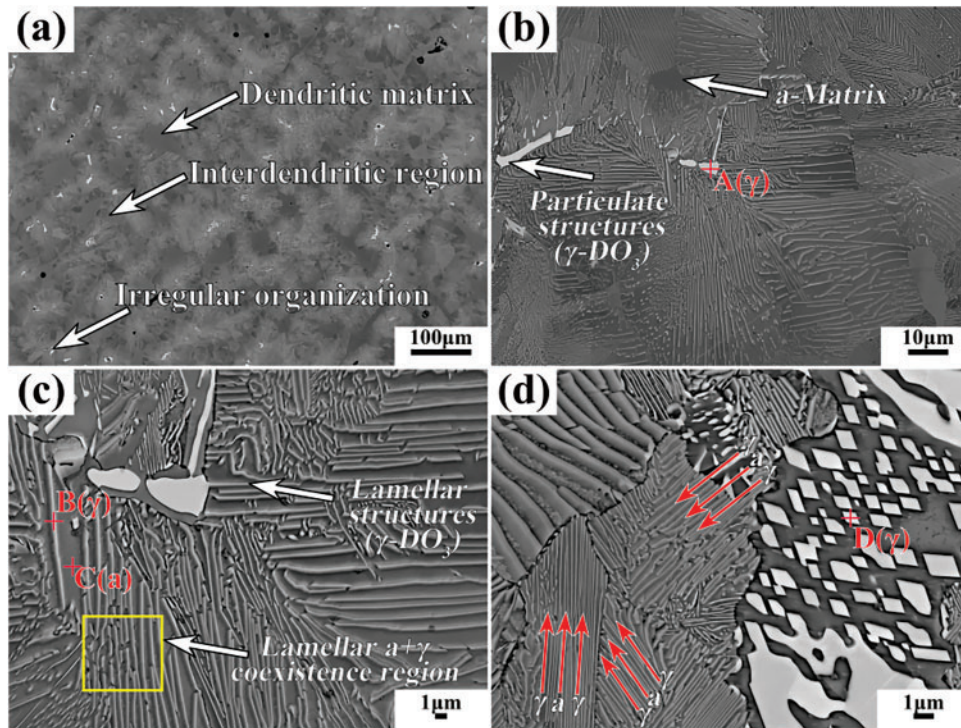
Figure 7: Microstructure of as-cast Cu-15Ni-8Sn alloys at different magnifications: (a) 150×, (b) 1000×, (c) 3000×, and (d) 5000×

Table 6: The EDS point findings for the respective locations shown in Fig. 7b–d

Region	at.%			wt.%		
	Cu	**Ni**	**Sn**	**Cu**	**Ni**	**Sn**
Point A	32.1	42.9	25.0	27.11	33.46	39.44
Point B	66.9	22.5	10.6	62.24	19.33	18.42
Point C	83.8	12.7	3.5	82.10	11.49	6.41
Point D	34.1	39.6	26.3	28.46	30.53	41.01

4 Conclusion

In this study, the Cu-Ni-Sn ternary system 2NN MEAM potential was developed, and used to simulate and calculate the relevant property parameters of the compound, the melting temperature of the Cu-15Ni-8Sn alloy, XRD patterns, and the Sn segregation at grain boundaries. The results were consistent with the DFT calculation and experiments, respectively. In summary, Cu-Ni-Sn ternary system 2NN MEAM potential presented in this article demonstrates excellent applicability in simulating the melting and solidification processes of Cu-15Ni-8Sn alloys, thereby facilitating the development of a perfect potential for the Cu-Ni-Sn system and its microalloying systems.

Author Contributions: The authors confirm contribution to the paper as follows: study conception and design: Jialiang Dong; data collection: Xuemao Dong; analysis and interpretation of results: Zhongxue Feng; draft manuscript preparation: Jialiang Dong and Zhongxue Feng; software, methodology: Caiju Li and Jianhong Yi; writing, review and editing: Zhongxue Feng and Jun Tan. All authors reviewed the results and approved the final version of the manuscript.

Availability of Data and Materials: The raw/processed data required to reproduce these findings cannot be shared at this time, as the data also form part of an ongoing study.

Ethics Approval: Not applicable.

Conflicts of Interest: The authors declare no conflicts of interest to report regarding the present study.

References

1. Yang M, Hu YL, Li XN, Li ZM, Zheng YH, Li NJ, et al. Compositional interpretation of high elasticity Cu–Ni–Sn alloys using cluster-plus-glue-atom model. J Mater Res Technol. 2022;17:1246–58. doi:10.1016/j.jmrt.2022.01.075.

2. Xie G, Wang Q, Mi X, Xiong B, Peng L. The precipitation behavior and strengthening of a Cu-2.0wt% Be alloy. Mater Sci Eng: A. 2012;558:326–30. doi:10.1016/j.msea.2012.08.007.

3. Eash JT, Upthegrove C. The copper-rich alloys of the copper-nickel-tin system. USA: University of Michigan; 1932 [cited 2024 Dec 30]. Available from: https://babel.hathitrust.org/cgi/pt?id=mdp.39015071604305.

4. Peng G, Gan X, Jiang Y, Li Z, Zhou K. Effect of dynamic strain aging on the deformation behavior and microstructure of Cu–15Ni–8Sn alloy. J Alloys Comp. 2017;718:182–7. doi:10.1016/j.jallcom.2017.05.127.

5. Zhang J, Wang Z, Miao S, Zhang Y, Fu Y, Dong Y, et al. Effect of defect strengthening on the mechanical properties of a novel Cu–15Ni–8Sn alloy. Mater Sci Eng: A. 2023;868:144777. doi:10.1016/j.msea.2023.144777.

6. Wang N, Shen Y, An Q, Reddy KM, Jin M, Karre R, et al. Microstructure evolution and mechanical property of Cu-15Ni-8Sn-0.2Nb alloy during aging treatment. J Mater Sci Technol. 2021;86:227–36. doi:10.1016/j.jmst.2021.01.034.

7. Guo Z, Jie J, Liu S, Zhang Y, Qin B, Wang T, et al. Effect of V addition on microstructures and mechanical properties of Cu-15Ni-8Sn alloy. Mater Sci Eng: A. 2019;748(9):85–94. doi:10.1016/j.msea.2019.01.084.

8. Li J, Zhang Z, Xu W, Yang Y, Xue P, Teng Q, et al. Hot isostatic pressing of Cu–15Ni–8Sn alloy with suppressed Sn macro-segregation and enhanced mechanical properties. Mater Sci Eng: A. 2022;855(5):143866. doi:10.1016/j.msea.2022.143866.

9. Perdew JP, Zunger A. Self-interaction correction to density-functional approximations for many-electron systems. Phys Rev B. 1981;23(10):5048. doi:10.1103/PhysRevB.23.5048.

10. Fracchia F, Del Frate G, Mancini G, Rocchia W, Barone V. Force field parametrization of metal ions from statistical learning techniques. J Chem Theory Comput. 2018;14(1):255–73. doi:10.1021/acs.jctc.7b00779.

11. Thompson MW, Gilmer JB, Matsumoto RA, Quach CD, Shamaprasad P, Yang AH, et al. Towards molecular simulations that are transparent, reproducible, usable by others, and extensible (TRUE). Mol Phys. 2020;118(9–10):e1742938. doi:10.1080/00268976.2020.1742938.

12. Jang HS, Seol D, Lee BJ. Modified embedded-atom method interatomic potentials for Mg–Al–Ca and Mg–Al–Zn ternary systems. J Magnes Alloys. 2021;9(1):317–35. doi:10.1016/j.jma.2020.09.006.

13. Mahata A, Mukhopadhyay T, Asle Zaeem M. Modified embedded-atom method interatomic potentials for Al-Cu, Al-Fe and Al-Ni binary alloys: from room temperature to melting point. Comput Mater Sci. 2022;201:110902. doi:10.1016/j.commatsci.2021.110902.

14. Zhou H, Dickel D, Baskes MI, Mun S, Asle Zaeem M. A modified embedded-atom method interatomic potential for bismuth. Modelling Simul Mater Sci Eng. 2021;29(6):065008. doi:10.1088/1361-651X/ac095c.

15. Wang J, Lee BJ. Second-nearest-neighbor modified embedded-atom method interatomic potential for V-M (M = Cu, Mo, Ti) binary systems. Comput Mater Sci. 2021;188(10):110177. doi:10.1016/j.commatsci.2020.110177.

16. Jang HS, Seol D, Lee BJ. Modified embedded-atom method interatomic potential for the Mg-Zn–Ca ternary system. Calphad. 2019;67:101674. doi:10.1016/j.calphad.2019.101674.

17. Muralles M, Oh JT, Chen Z. Molecular dynamics study of FeCo phase transitions and thermal properties based on an improved 2NN MEAM potential. J Mater Res Technol. 2022;19:1102–10. doi:10.1016/j.jmrt.2022.05.100.

18. Weng Z, Zhang F, Xu C, Zhou J. The effect of incident energy, incident angle and substrate temperature on surface morphology and atomic distribution of NiTi films. Mater Des. 2020;187:108350. doi:10.1016/j.matdes.2019.108350.

19. Lee BJ, Shim JH. A modified embedded atom method interatomic potential for the Cu-Ni system. Calphad. 2004;28(2):125–32. doi:10.1016/j.calphad.2004.06.001.

20. Kim Y, Lee BJ. Second nearest-neighbor modified embedded atom method interatomic potentials for Na-M–Sn (M = Cu, Mn, Ni) ternary systems. Comput Mater Sci. 2022;206(38):111305. doi:10.1016/j.commatsci.2022.111305.

21. Ko WS, Lee JS, Kim DH. Atomistic simulations of Ag–Cu–Sn alloys based on a new modified embedded-atom method interatomic potential. J Mater Res. 2022;37(1):145–61. doi:10.1557/s43578-021-00395-z.

22. Aguilar JF, Ravelo R, Baskes MI. Morphology and dynamics of 2D Sn-Cu alloys on (100) and (111) Cu surfaces. Modelling Simul Mater Sci Eng. 2000;8(3):335–44. doi:10.1088/0965-0393/8/3/313.

23. Lee BJ, Shim JH, Baskes MI. Semiempirical atomic potentials for the FCC metals Cu, Ag, Au, Ni, Pd, Pt, Al, and Pb based on first and second nearest-neighbor modified embedded atom method. Phys Rev B. 2003;68(14):144112. doi:10.1103/PhysRevB.68.144112.

24. Ko WS, Kim DH, Kwon YJ, Lee M. Atomistic simulations of pure tin based on a new modified embedded-atom method interatomic potential. Metals. 2018;8(11):900. doi:10.3390/met8110900.

25. Lee BJ, Baskes MI. Second nearest-neighbor modified embedded-atom-method potential. Phys Rev B. 2000;62(13):8564–7. doi:10.1103/PhysRevB.62.8564.

26. Lee BJ, Baskes MI, Kim H, Koo Cho Y. Second nearest-neighbor modified embedded atom method potentials for bcc transition metals. Phys Rev B. 2001;64(18):184102. doi:10.1103/PhysRevB.64.184102.

27. Rose JH, Smith JR, Guinea F, Ferrante J. Universal features of the equation of state of metals. Phys Rev B. 1984;29(6):2963–9. doi:10.1103/PhysRevB.29.2963.

28. Asadi E, Asle Zaeem M, Nouranian S, Baskes MI. Two-phase solid-liquid coexistence of Ni, Cu, and Al by molecular dynamics simulations using the modified embedded-atom method. Acta Mater. 2015;86:169–81. doi:10.1016/j.actamat.2014.12.010.

29. Baskes MI. Application of the embedded-atom method to covalent materials: a semiempirical potential for silicon. Phys Rev Lett. 1987;59(23):2666–9. doi:10.1103/PhysRevLett.59.2666.

30. Baskes MI. Determination of modified embedded atom method parameters for nickel. Mater Chem Phys. 1997;50(2):152–8. doi:10.1016/S0254-0584(97)80252-0.

31. Kim KH, Jeon JB, Lee BJ. Modified embedded-atom method interatomic potentials for Mg–X (X=Y, Sn, Ca) binary systems. Calphad. 2015;48:27–34. doi:10.1016/j.calphad.2014.10.001.

32. Kim YM, Lee BJ. A modified embedded-atom method interatomic potential for the Cu-Zr system. J Mater Res. 2008;23(4):1095–104. doi:10.1557/jmr.2008.0130.

33. Xiang H, Guo W. A newly developed interatomic potential of Nb–Al–Ti ternary systems for high-temperature applications. Acta Mechanica Sinica. 2022;38(1):121451. doi:10.1007/s10409-022-09007-x.

34. Kim HK, Jung WS, Lee BJ. Modified embedded-atom method interatomic potentials for the Fe–Ti–C and Fe–Ti–N ternary systems. Acta Mater. 2009;57(11):3140–7. doi:10.1016/j.actamat.2009.03.019.

35. Kim HK, Jung WS, Lee BJ. Modified embedded-atom method interatomic potentials for the Nb-C, Nb-N, Fe-Nb-C, and Fe-Nb-N systems. J Mater Res. 2010;25(7):1288–97. doi:10.1557/JMR.2010.0182.

36. Ko WS, Lee BJ. Modified embedded-atom method interatomic potentials for pure Y and the V–Pd–Y ternary system. Modelling Simul Mater Sci Eng. 2013;21(8):085008. doi:10.1088/0965-0393/21/8/085008.

37. Wu C, Lee BJ, Su X. Modified embedded-atom interatomic potential for Fe-Ni, Cr-Ni and Fe-Cr-Ni systems. Calphad. 2017;57:98–106. doi:10.1016/j.calphad.2017.03.007.

38. Plimpton S. Fast parallel algorithms for short-range molecular dynamics. J Comput Phys. 1995;117(1):1–19. doi:10.1006/jcph.1995.1039.

39. Stukowski A. Visualization and analysis of atomistic simulation data with OVITO-the Open Visualization Tool. Modelling Simul Mater Sci Eng. 2010;18(1):015012. doi:10.1088/0965-0393/18/1/015012.

40. Kresse G, Furthmüller J. Efficient iterative schemes for ab initio total-energy calculations using a plane-wave basis set. Phys Rev B Condens Matter. 1996;54(16):11169–86. doi:10.1103/PhysRevB.54.11169.

41. Kresse G, Furthmüller J. Efficiency of ab-initio total energy calculations for metals and semiconductors using a plane-wave basis set. Comput Mater Sci. 1996;6(1):15–50. doi:10.1016/0927-0256(96)00008-0.

42. Kresse G, Hafner J. Ab initio molecular-dynamics simulation of the liquid-metal-amorphous-semiconductor transition in germanium. Phys Rev B Condens Matter. 1994;49(20):14251–69. doi:10.1103/PhysRevB.49.14251.

43. Blöchl PE. Projector augmented-wave method. Phys Rev B Condens Matter. 1994;50(24):17953–79. doi:10.1103/PhysRevB.50.17953.

44. Perdew JP, Burke K, Ernzerhof M. Generalized gradient approximation made simple. Phys Rev Lett. 1996;77(18):3865–8. doi:10.1103/PhysRevLett.77.3865.

45. Zhao JC, Notis MR. Spinodal decomposition, ordering transformation, and discontinuous precipitation in a Cu–15Ni–8Sn alloy. Acta Materialia. 1998;46(12):4203–18. doi:10.1016/S1359-6454(98)00095-0.

46. Murnaghan FD. The compressibility of media under extreme pressures. Proc Natl Acad Sci U S A. 1944;30(9):244–7. doi:10.1073/pnas.30.9.244.

47. Birch F. Finite elastic strain of cubic crystals. Phys Rev. 1947;71(11):809–24. doi:10.1103/PhysRev.71.809.

48. Separdar L, Rino JP, Zanotto ED. Molecular dynamics simulations of spontaneous and seeded nucleation and theoretical calculations for zinc selenide. Computat Mater Sci. 2021;187(48):110124. doi:10.1016/j.commatsci.2020.110124.

49. Luo SN, Strachan A, Swift DC. Nonequilibrium melting and crystallization of a model Lennard-Jones system. J Chem Phys. 2004;120(24):11640–9. doi:10.1063/1.1755655.

50. Sankaranarayanan SKRS, Bhethanabotla VR, Joseph B. Molecular dynamics simulation study of the melting of Pd-Pt nanoclusters. Phys Rev B. 2005;71(19):195415. doi:10.1103/PhysRevB.71.195415.

51. Luo SN, Ahrens TJ, Çağın T, Strachan A, Goddard WA, Swift DC. Maximum superheating and undercooling: systematics, molecular dynamics simulations, and dynamic experiments. Phys Rev B. 2003;68(13):134206. doi:10.1103/PhysRevB.68.134206.